2019

A Microfocal Effect In Photoreceptor Light Capture

Vasantha Kumari Kanukuntla
University of Alabama at Birmingham

A MICROFOCAL EFFECT IN PHOTORECEPTOR LIGHT CAPTURE

by

VASANTHA K. KANUKUNTLA

LAWRENCE C. SINCICH, COMMITTEE CHAIR
JOHN M. LAURENT
LEI LIU

A THESIS

Submitted to the graduate faculty of The University of Alabama at Birmingham,
in partial fulfillment of the requirements for the degree of
Master of Science

BIRMINGHAM, ALABAMA

2019

A MICROFOCAL EFFECT IN PHOTORECEPTOR LIGHT CAPTURE

VASANTHA K. KANUKUNTLA

MASTERS OF SCIENCE IN VISION SCIENCE

ABSTRACT

In human eyes, accomodation brings light rays into focus on the retina in order to achieve a clear images. The plane of best focus within the depth of the retina is thought to be within the photoreceptor layer, but pinpointing the exact focal position axially has not been determined. With help of adaptive optics aberration correction and its ability to have microscopic control of a retinal stimulus, we explored how sensitive human subjects are to defocus on the micron scale. We found that focal position can be reliably judged within 0.02 D, which is equivalent to about 6 microns in axial depth for a human eye.

DEDICATION

I would like to dedicate my thesis to all my family members. My husband and Kids, my parents and siblings to whom I owe everything. My husband who always believed in me, encouraged me and supported me to achieve my career goals. My parents and siblings who always showed their unconditional love and support. My kids who had to compromise in many aspects during the busy period of my educational journey. Though few sentences won't be adequate to describe their sacrifices, love and support, I hope they know how much love and affection I have towards them.

ACKNOWLEDGEMENTS

First, I would like to thank Dr. Lawrence Sincich. Thank you for being such a wonderful mentor. This would have not been possible without you and I am truly honored to work with you. I want to express my deepest gratitude for believing in me and I truly appreciate and value everything I have learned from you. Thank you for your time, support, guidance and your patience. I am proud to say that I am your first graduating Masters student in Vision Science.

To my committee members Dr. Lei Lui and Dr. John M. Laurent: Thank you for all your time and support and thank you for being part of this project. It's an honor to complete this degree under your leadership and guidance.

I would like to thank Dr. Alexander Meadway and Dr. Philipp Tellers for helping me through the experiments in the lab. I am grateful for your time and support.

I would like to thank all the study participants for your precious time and your contributions to science and research.

TABLE OF CONTENTS

Page

LIST OF FIGURES

LIST OF ABBREVIATIONS

AO: Adaptive optics.

AOSLO: Adaptive optics Scanning Laser Ophthalmoscope.

LCA: Longitudinal Chromatic aberration

TCA: Transverse Chromatic aberration

ELM: External limiting membrane.

CCD: Charge-coupled device

MEMS: Micro-electro-mechanical system.

INTRODUCTION

Vision is an important sense and the process is initiated by the eye which is the first organ in the visual system. The eye is a modest optical instrument with two positive lenses (the cornea and the crystalline lens) that form images on the retina as the first step in vision. Photoreceptors are sensors of the visual system that capture the photons of light and generate a signal that is transmitted to the visual cortex for further processing. Various advances in retinal imaging have made it possible to view retinal structures at cellular level. Adaptive optics (AO) retinal imaging recently enabled direct visualization of individual rod and cone photoreceptors in the living eye which helps us to understand how vision works (Williams 2011). By incorporating the ability to have microscopic control of a retinal stimulus, AO also allows us to explore and analyze the light capture in photoreceptors (Roorda 2011). The aim of this thesis is to use AO methods to determine how sensitive human subjects are to defocus in the axial direction of the retina on the micron scale.

Optical Properties of the Eye

The path of the light traversing the eye is affected by many ocular structures that can influence image quality. The light is first refracted by the cornea which is steeper centrally with an average thickness of 0.55 mm and flatter in the periphery, averaging 0.71 mm in thickness and 12 mm in horizontal diameter (Remington 2012; other ocular

quantities listed below are from the same citation). The mean radius of curvature of the central cornea at the anterior surface is 7.8 mm and the posterior surface is 6.5 mm with a refractive index of 1.377. The unaccommodated eye has an approximate optical power of 60 D with corneal power being approximately 40 D which is about 67% of the total refractive power of the eye. This is mainly due to the large difference in refractive index between the air and the precorneal tear film. Due to avascularity and orderly arrangement of collagen fibrils in the cornea, it is highly transparent with transmission above 95% in the spectral range of 400-900 nm. Consequently, it becomes the principal refractive component of the eye. The precorneal tear film on the cornea ensures a smooth optical surface to improve the image quality. Behind the cornea lies the anterior chamber, filled with the aqueous humor, a water-like substance having a refractive index $n \approx 1.334$. The defining aperture of the eye, the pupil, is the opening in the center of the iris and its size is controlled by two sets of muscles. The pupil size changes with the light levels, from less than 2 mm in diameter in intense light to more than 8 mm in dark conditions, thus controlling retinal illumination by limiting the light entering the eye, which in turn affects the retinal image quality.

After passing through the iris, light next encounters the crystalline lens, which is biconvex with anterior radius of curvature of 8-14 mm and posterior radius of 5-8 mm. The internal structure of the lens is layered, leading to a non-homogeneous refractive index, higher in the center than in the periphery, and with an approximate equivalent value of 1.42. The lens is ~4 mm in thickness and ~10 mm in diameter, enclosed within a tough, thin (5-15 μm), collagenous capsule attached by ligaments called zonnules to the ciliary body. Muscles in the ciliary body permit the lens to increase or decrease in power.

The lens in a relaxed eye has a power of about 20 D, while in the fully accommodated state, it can transiently increase to 33 D.

Posterior to the lens lies the vitreous humour, gel-like substance with a refractive index of ~1.336. These transparent optical elements with specified power, transparency and selective refractive indices bend light rays to form images of the world on the retina.

An average eye has an anterior chamber depth of 3.05 mm, lens thickness of 4 mm, and posterior chamber of 16.6 mm which leads to a total axial length of 24.2 mm. When the combined power of the refractive elements of the eye are just right for the axial length, the image of distant scenes eye will be in focus on the retina without accomodation (Artal 2016). This condition is emmetropia. Not surprisingly, most eyes have refractive errors because of blemishes in their optical properties or not having the exact dimensions required for perfect focus. When eyes are at perfect focus, as in an ideal emmetrope, still they do not produce diffraction-limited images. Consequently the retinal image of a point source is a distorted and extended distribution of light rather than another point. Such degradation of retinal images is due to diffraction by the eye's pupil, optical aberrations, and intraocular scattering. Diffraction naturally blurs images that pass through a limited aperture, a consequence of the wave nature of the light.

Image Forming Properties

The image forming quality of any optical system, including the eye, can be described completely by the shape of the transmitted wavefront for a given wavelength of light. It is defined as the difference between the perfect and the actual wave fronts

encountered at every point over the eye's pupil (Artal 2016). A perfect eye would form an undistorted retinal image of a point source (an Airy disk), though such perfection never occurs naturally (Thibos *et al*. 2002; Salmon & van de Pol 2006). Any imperfections in an optical system are usually characterized as wavefront aberrations, and their presence generates distortions in the retinal image. Wavefront aberrations consist of both low-order aberrations like positive defocus (myopia), negative defocus (hyperopia) and regular astigmatism which can be corrected with spectacles, and high-order aberrations like coma, trefoil, and spherical aberration are not correctable with spectacles. High-order aberrations as a group still amount to perceptible degrees of optical distortion. The cornea and lens due to their shapes correct some amount of aberrations. But this is possible only in younger eyes, because with increase in age there will be increased aberrations due reduced transparency in various ocular structures. Also, the eye acts like an aplanatic optical system with partial correction of the aberrations, which may help to maintain stable optical quality.

The severity of monochromatic aberrations in human eyes depend on variety of factors like individual variation, pupil size, refractive error, accommodation, aging and retinal eccentricity. On average, the summed high-order aberrations have a root-mean squared (RMS) value of 0.33 μm, equivalent to 0.25 D of defocus (Thibos *et al*. 2002; Salmon & van de Pol 2006). A higher RMS value indicates a more highly aberrated cornea. There is an increase in aberrations as the pupil becomes larger, with RMS error approximately doubling with each additional millimeter of mydriasis.

For the purposes of this study, we needed to measure as well as correct these high-order aberrations of the eye. They can be measured using variety of wave front

sensing techniques, both subjective and objective: Vernier alignment, the Foucault knife edge technique, a cross cylinder aberroscope, calculations from double pass retinal images, the pyramid sensor, and the most commonly used, the Shack-Hartmann wavefront sensor (Artal 2016). As described in the General Methods section, we used Shack-Hartmann wavefront sensing to measure the wavefront in our subjects, while adaptive optics techniques were used to correct those aberrations. Despite these corrections, there are two types of relevant aberrations that cannot be corrected with adaptive optics and they are described next.

Chromatic aberrations in optical systems are caused by chromatic dispersion, the dependence of refractive index on wavelength. Chromatic aberration is traditionally divided into longitudinal and transverse chromatic aberration (LCA and TCA, respectively). LCA is the variation of axial power with wavelength, which leads to a change in focus, while TCA is the lateral shift of the image across the image plane for all points not lying on the optical axis, which leads to a change in magnification as well as different retinal image position. Both LCA and TCA needed to be taken into account for our experiments (Harmening *et al*., 2012).

LCA in the human eye is relatively constant between individuals. Thus LCA can be corrected by static adjustment of the focus any light sources with different wavelengths using a mathematical fit to compiled human population data. By selecting one wavelength to be emmetropic in the system (currently this is the red channel at 710 nm, a wavelength in the middle of the other two light channels), we can minimize the relative defocus between channels. So this correction was −0.69 D for our 543 nm

channel (green), and +0.30 D for our infrared imaging channel of 840 nm (Harmening *et al*., 2012).

TCA is mainly caused by misalignment of the imaging beam relative to the eye's achromatic axis (along which TCA is zero by definition). TCA correction is very challenging because, finding the achromatic axis is very difficult. It is known that the position of achromatic axis relative to the pupil is highly idiosyncratic so we need to find this axis for each eye empirically. Also the eye is always in motion, even when a subject attempts to fixate, so TCA is always changing and it varies based on retinal eccentricity. Hence during multiwavelength light delivery in the living eye it is very important to measure and correct TCA when the intent is to target single cones for stimulation (as in our Experiment 2).

One other source of potential chromatic offset is any residual uncorrected optical misalignments of the three wavelength channels in the AO instrument itself (see General Methods below). These offsets are technically hard to avoid completely. TCA offsets in an LCA corrected imaging system are due to lateral shifts of the subject's pupil relative to the imaging beam. The lateral pupil displacements of 0.25 mm produce TCA changes about twice as large as the smallest cones in the fovea for the green channel (Harmening *et al*., 2012). Even with small pupil displacements during gaze shifts or head movements, there is a considerable change in TCA offsets. But as long as the subject's head position (stabilized with a bite bar) and fixation point are not changed, TCA measurements with practiced subjects do not shift by more than 2 pixels in an image frame 512 pixels wide (Harmening *et al*, 2014).

Photoreceptor Organization of the Retina

The retina is the tissue that converts light into visual signals transmitted to the brain. This process is accomplished by two types of photoreceptors (rods and cones) which are the sensors of the visual system, capturing photons of light and converting them into a neural signal in a process called phototransduction. The rods and cones are distinguished by shape, type of photopigment, retinal topographic distribution, and pattern of synaptic connections. These properties make the rod and cone systems specialized for different visual tasks. The rod system has low spatial resolution but is sensitive to light at the single photon level. In contrast, the cone system has high spatial resolution but is much less sensitive to light. Thus, cones are specialized for photopic visual acuity at the expense of sensitivity.

The human retina contains in the range of 4-5 million cones and 70–100 million rods. Only cones are found in the foveola, while rods outnumber cones outside the foveola and throughout the peripheral retina. The cone inner segment diameters become larger and density declines rapidly with eccentricity. Images of cones near the fovea show occasional hexagonal packing but with increasing retinal eccentricity cones are not in contiguous apposition anymore because of intervening rods (Curcio *et al.*, 1990). Cones have a higher density along the horizontal (temporal, nasal) meridians than along the vertical (superior, inferior) meridians as seen in histological samples (Hirsch and Curcio 1989; Curcio *et al*. 1990) and with *in vivo* imaging (Chui, Song & Burns, 2008; Song *et al*., 2011; Zhang, *et al*., 2015).

The central fovea with highest cone density yields the highest perceptual spatial resolution; however, even the retinal periphery plays a crucial role in our visual system. When object are presented peripherally, the eye's optics operate differently. Oblique rays generate off-axis aberrations, which in turn compromises the ability to discriminate small objects. For example, resolution at the fovea is normally 1 arcmin, but it increases to 2.5, 5, and 10 arcmin at 10°, 20°, and 30° of eccentricity, respectively (Artal, 2016). This reduction in resolution is due to optical as well as neural factors: any eccentric angular incidence induces optical aberrations, which lowers the contrast of the retinal images, and as the density of cones and ganglion cells declines with eccentricity, this results in sparser neural sampling of any image. As seen in our experiments, dramatically differently sized stimuli were required for generating percepts between foveal and parafoveal eccentricities.

If we look at the structure of the photoreceptors, cone inner segments are smallest in diameter at the fovea become larger with increasing distance from the fovea (Polyak, 1941; Yamada, 1969). Cone inner segments are ~2.5 μm in diameter at the center of the fovea, increasing to ~8 μm at 20° degrees eccentricity, eventually reaching over 11 μm at the edge of the temporal retina. Outer segment lengths also vary as a function of retinal location (Polyak 1957; Hendrickson & Yuodelis, 1984), being about 70 μm at the center of the fovea and approaching 50 μm in the periphery. Good visual sensitivity is based on photon capture being efficient, isomerizing as much photopigment as possible, which is expected to occur when focus is optimal.

Photoreceptors as Waveguides and Light Collectors

Optically, the capture of light is not simply a factor of how many photons impinge upon the photoreceptor. Light capture efficiency is influenced by the shape of the photoreceptors as well as the direction of incoming beams. It has been found that cones appear to sum light over a Gaussian aperture that is smaller than one cone inner segment diameter (MacLeod, Williams & Makous, 1992). This occurs because photoreceptors act as optical fibers, exhibiting wave guided behavior that entails discrete light acceptance apertures in each cone and gives rise to angular sensitivity tuning in the retina (Enoch & Tobey, 1981). Since the index of refraction of the inner and outer segments is higher than the surrounding extracellular medium (Sidman, 1957), total internal reflection can occur. If a beam enters the photoreceptor over a small set of angles, much of the light will remain within the receptor as it acts as an optical waveguide (Snyder & Pask, 1973). The high refractive index of the inner segment is likely due to densely packed mitochondria (Enoch, 1961; Rowe *et al*., 1994). Funneling of light by inner segments is also improved by their shape (Burns *et al*., 1997; Meadway & Sincich, 2018). Peripheral cones have relatively large inner segments (Packer *et al*., 1989), so they can direct more light into the narrow outer segment (Miller & Snyder, 1973; Meadway & Sincich 2018). The Stiles-Crawford effect is a direct consequence of the directional waveguiding in optical fibers (Rodieck, 1973). Light entering near the pupil edge is less effectively captured because it enters the inner segment at a steeper angle and so less light passes into the outer segment. Where cones are longer, as in the fovea, there is less sensitivity to light directionality compared to the more tapered parafoveal cones (Westheimer, 1967; Burns *et al*., 1997).

There is now considerable evidence that waveguiding is an important factor in photoreceptor light capture, and this thesis aims to examine its impact on defocus sensitivity.

The eye functions best when it has a sharply focused image on its retina. Spatially, this means that neighboring photoreceptors are registering the largest difference in light capture, which is equivalent to highest image contrast. Image contrast is in the plane of the retina. But focus is an axial parameter, so focus in depth also impacts the relative light capture of neighboring photoreceptors, and thus alters contrast detection. This change in contrast as a function of focus becomes the key signal for accommodation (Glasser, 2011).

How the Eye Focuses and Prior Studies of Accommodation Sensitivity

Accommodation is a process whereby the eye changes the power of its lens to enable it to focus on objects over a wide range of distances. There are both objective and subjective measures of accommodation. Objectively, accommodation can be measured with the help of, optometer, aberrometers, or auto-refractors. Subjective measures depend on a person's ability to appreciate the blur as the target is moved away from the plane of fixation. This subjective means of measuring accommodation overestimates the accommodative amplitude due to the depth of field of the eye (Glasser, 2011). For optometric purposes, the range of distances over which a subject cannot detect any difference in focus is called depth of field. This range may be specified by the movement of the object plane or by the corresponding movement of the image plane. Some authors

differentiate depth of field as movement of object plane and depth of focus as movement of image plane. But quantitatively, depth of focus and depth of field are interchangeable when measured in diopters.

Subjective depth of focus is constitutively larger than objective depth of focus, with subjective depth of focus increasing with age in part due to the decrease in pupil diameter and increased subjective tolerance to defocus or blur (Wang & Ciuffreda, 2005). An subject's perception of blur depends on two factors: (1) a physiological factor determined by perceptual tolerance to blur, related to the size and distribution of photoreceptors on the retina, along with factors like the Stiles-Crawford effect, and (2) optical factors which are responsible for focusing the light on the retina. The depth of field depends on various factors, including (1) optical properties like pupil size and aberrations within the eye, (2) target properties like illumination of the object, spatial detail, spectral properties, and contrast, and (3) retinal and visual processing properties like photoreceptor size and ganglion cell density, visual acuity, and any ocular pathology. For example, depth of focus is considerably greater in the peripheral retina than in the fovea, because of the lower density of cones. Foveally, defocus is drives the experience of visual blur. The human eye often suffers from errors of refraction and other optical aberrations leading to accumulating degrees of blur. The visual system does not detect blur until the magnitude of defocus exceeds some perceptually tolerable range. Previous studies have shown a wide range of total depth of focus at the fovea (at the extremes subjects can tolerate 0.04 D to 3.50 D), but the typical values are 0.8 D to 1.2 D in young and experienced observers (Wang & Ciuffreda, 2006). Using laser speckle as a guage,

minimum depth of focus was noted to be ±0.3 D under optimal conditions with a 3 mm pupil in normal eyes (Charman & Whitefoot, 1977).

The accommodative mechanisms can rely on many cues to focus the retinal image. Stimulus-driven accommodation is usually based on retinal blur, arising from erroneous optical vergence. The natural environment is rich in binocular, monocular, and spatial cues like size disparity and chromatic and monochromatic aberrations. Each of these can contribute to the estimates of signs of defocus, allowing accommodation to respond in the appropriate direction to focus with minimal errors. Higher order aberrations can also cause a difference in the appearance of stimuli at distances nearer and farther from best focus that could serve as a signed error signal for accommodation. Higher order aberrations could also exacerbate the accommodative response because they increase the depth of focus is larger (Chen *et al*., 2006). So when we use adaptive optics to correct the higher order aberrations, the depth of focus is reduced; thus objects that lie nearer or farther from the plane of focus will be perceived as having worse image quality than when the aberrations are left uncorrected (Chen *et al*., 2006). By using adaptive optics corrected stimuli we will be able to make focus steps on the order of 0.01 D after aberrations are corrected, thereby allowing us to test the sensitivity of human subjects to differences in microfocal steps in stimuli.

Normal accommodation sensitivity in the human eye has been measured for target movements as small as 0.1 D (Ludlam *et al.*, 1968), although this may not have been perceived by the subjects. As this degree of accommodation equals ~30 μm axially, this suggests that the eye is sensitive to focal changes shorter than the length of a cone photoreceptor (~60 μm for inner plus outer segment).

Optical Model of Light Capture Model and Predictions

Optical modeling of wave guiding in photoreceptors was recently developed to examine how light capture is influenced by cone morphology (Meadway & Sincich, 2018). Such modeling predicts that light capture in cones may vary for small changes in axial focus, down to the micron scale, in both parafoveal (Fig. 1) and foveal cones (Fig. 2). Moreover, such modeling predicts that there is one particular focal point where light absorption of a stimulus targeted to one photoreceptor will be maximized (Fig. 3, black line). Specifically, a focal point somewhere in the middle of the inner segment appears to produce maximal light coupling. The defocus position for peak light capture for a targeted cone is at the same location where the surrounding cones get the least light (Fig. 3, red line). As one moves away from this focal position, the difference in light capture between the targeted cone and its neighbors decreases. From a subject's point of view, however, they only perceive the summed light capture from all cones, leading to a modest difference in peak and minimum (Fig. 3, dashed line). This difference in light capture between peak and minimum is about 22% less light. As we will see in Experiment 2, this puts a limit on any subject's sensitivity to defocus if one is trying to measure differences in light capture directly.

For foveal cones, the situation is more dependent on stimulus size, wavelength and geometry. Because defocus is ultimately derived from differences in light capture between adjacent cones, we computed what this ratio would be as a function of defocus for foveal cones. For a point stimulus, the ratio is nearly 100:1 (Fig. 4, dashed line). However, our AOSLO microstimulator cannot deliver such a small stimulus. So we

computed what the capture ratio would be for a typical stimulus (5×5 pixel spot, see Experiment 3) presented at the fovea. When centered on a cone, the capture ratio is minimal because the stimulus directly hits both cones (Fig. 4, red line). If the edge of the stimulus lands between cones, the ratio can be quite high (Fig. 4, black line). This suggests that with proper stimulus positioning, a subject could perceive relatively high contrast. For this optimal condition, the predicted light capture falls to half-maximum in this model at a half-width of about 0.04 D, which implies that contrast between cones will fall by half within ~15 μm of the axial focal position in foveal cones. Since this cone contrast is what defines perceptual acuity, our experiments aim to determine if such a focal range is measurable in AO-corrected conditions. The various photoreceptor diameters and lengths used in these models were derived from summary data (Spaide & Curcio 2011; Meadway & Sincich 2018).

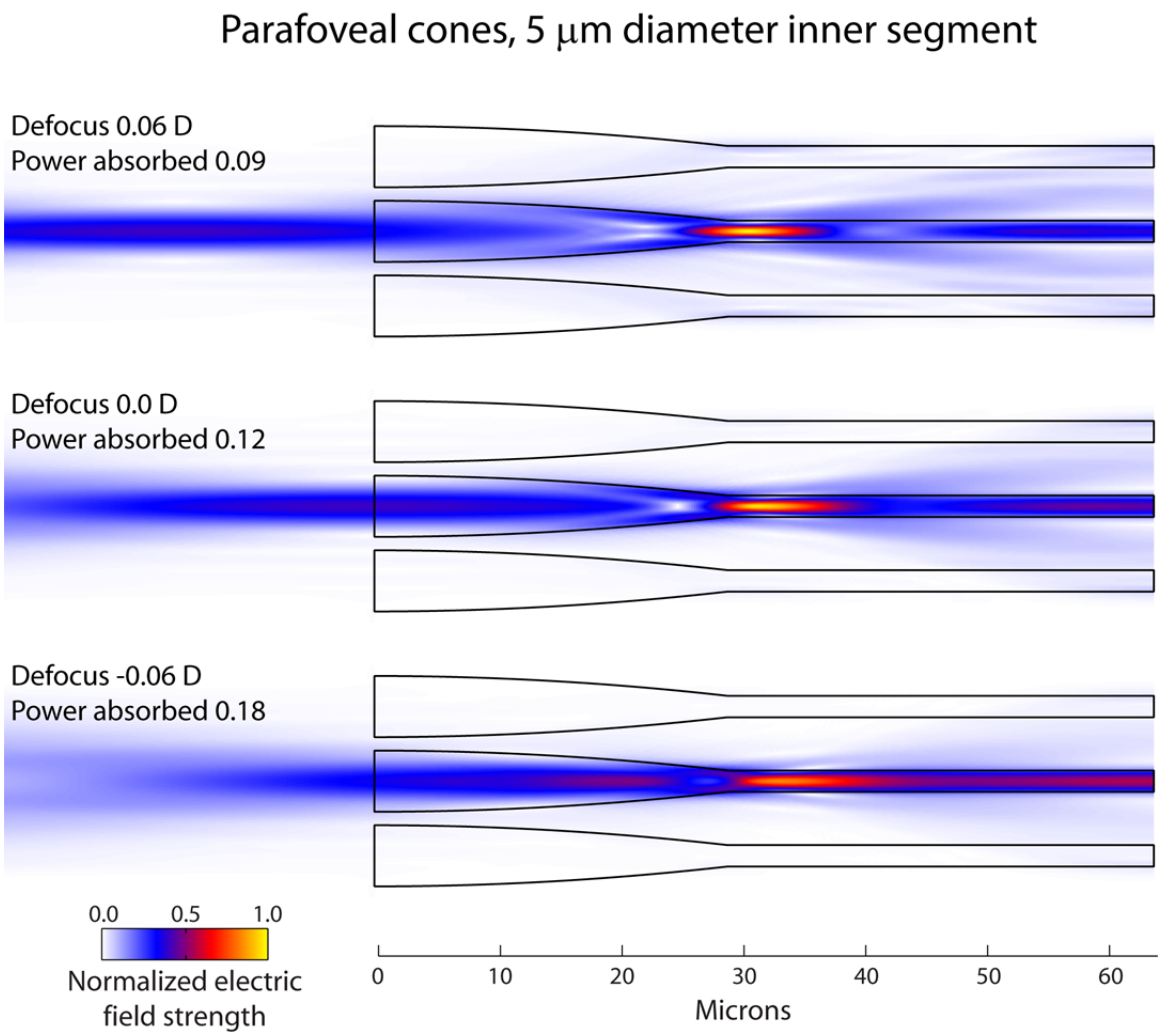

Figure 1. Axial light propagation in parafoveal cones as a function of defocus. Zero defocus is set to be at the external limiting membrane (ELM). Cone shape is outlined in black. The power absorbed is calculated for the entire central cone's outer segment, and is represented as a portion of the unit power input of 1. Optimal power absorption occurs in this example at a defocus of -0.06 D, which is ~18 μm into the inner segment of the cone. Field strength for all panels is normalized to the peak power value, which happens to occur in the 0.06 D case (top). Inner segment diameter is 5 μm at the ELM and outer segment diameter is 1.75 μm. Total length is 64 μm. Modeled wavelength was 543 nm.

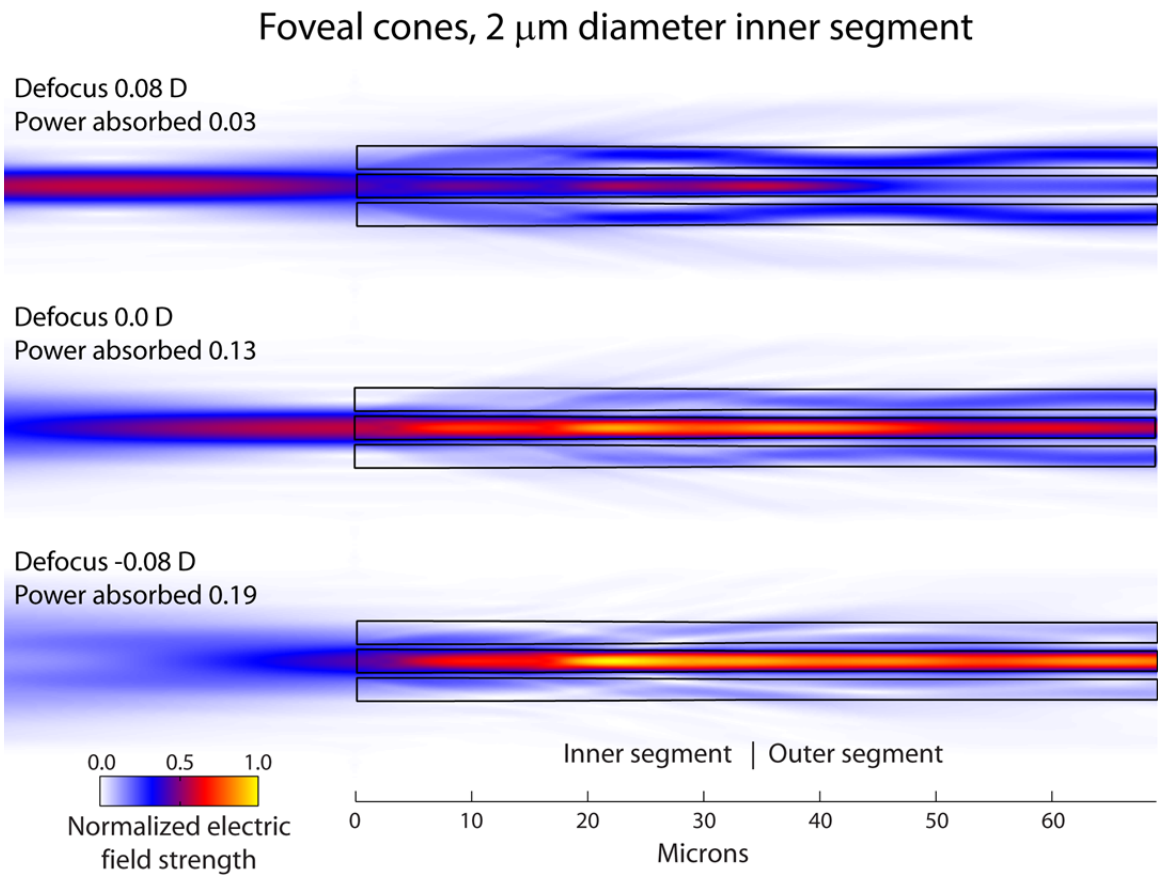

Figure 2. Axial light propagation in foveal cones as a function of defocus. Data are represented as in **Figure 1**. Foveal cone inner segments are nearly the same diameter as the outer segments, with the junction occurring at 34 μm from the ELM (as shown), so they exhibit much less tapering in shape and thereby less funneling of light into the outer segment. Optimal power absorption occurs in this example at a defocus of -0.08 D, which is ~24 μm into the inner segment of the central cone. Field strength for all panels is normalized to the peak power value.

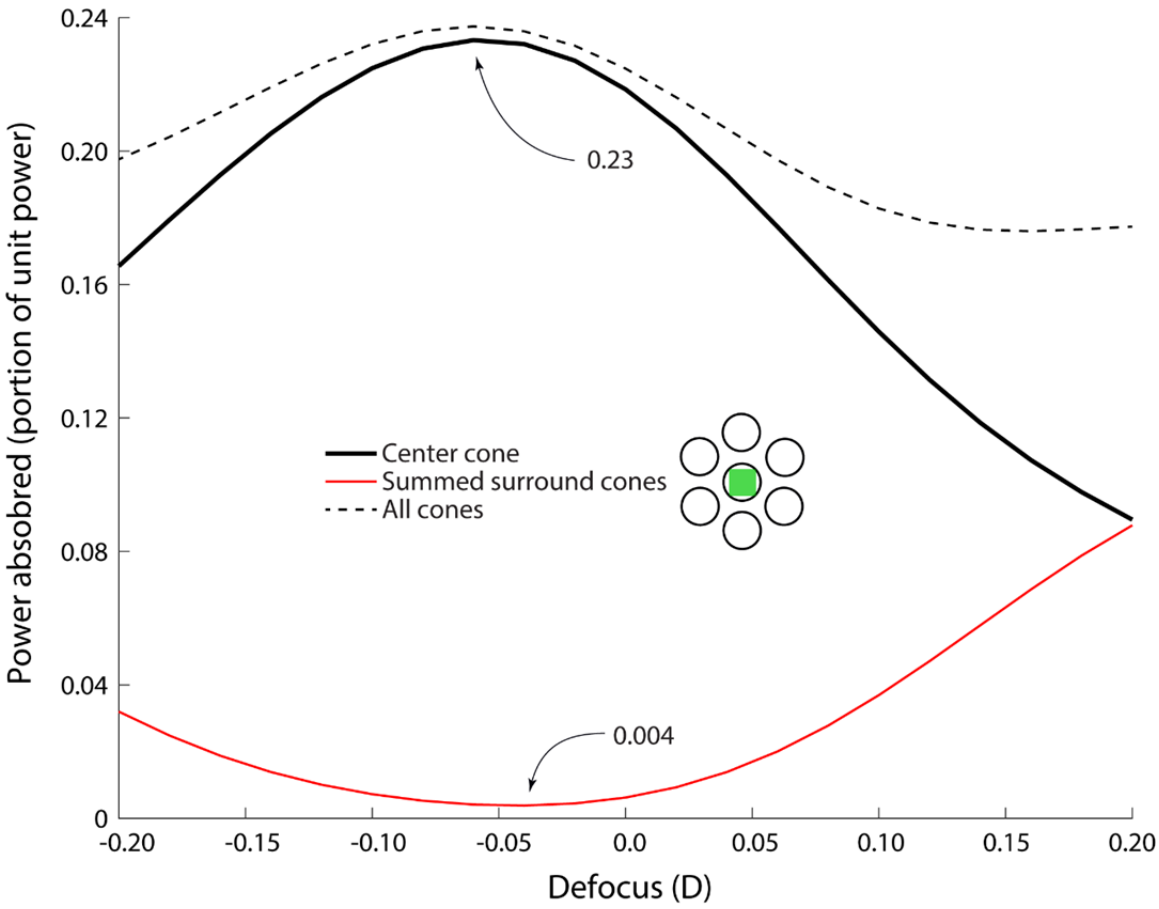

Figure 3. Light absorption in parafoveal cones varies as a function of defocus. Calculated power absorbed in a set of 7 cones, with a 5×5 pixel stimulus of 543 nm light placed on the center cone. These cones had 5 μm diameter inner segments, as in **Figure 1**. Absorbed power in the outer segment is represented as a portion of the unit power input of 1. Peak absorption for the center cone occurred at a defocus of -0.06 D, while the nadir in absorption summed across all 6 surround cones occurred with a defocus of -0.04 D relative to the ELM at 0.0 D. Negative defocus is behind the ELM and inside the inner segment, while positive defocus is in front of the photoreceptor toward the inner retina.

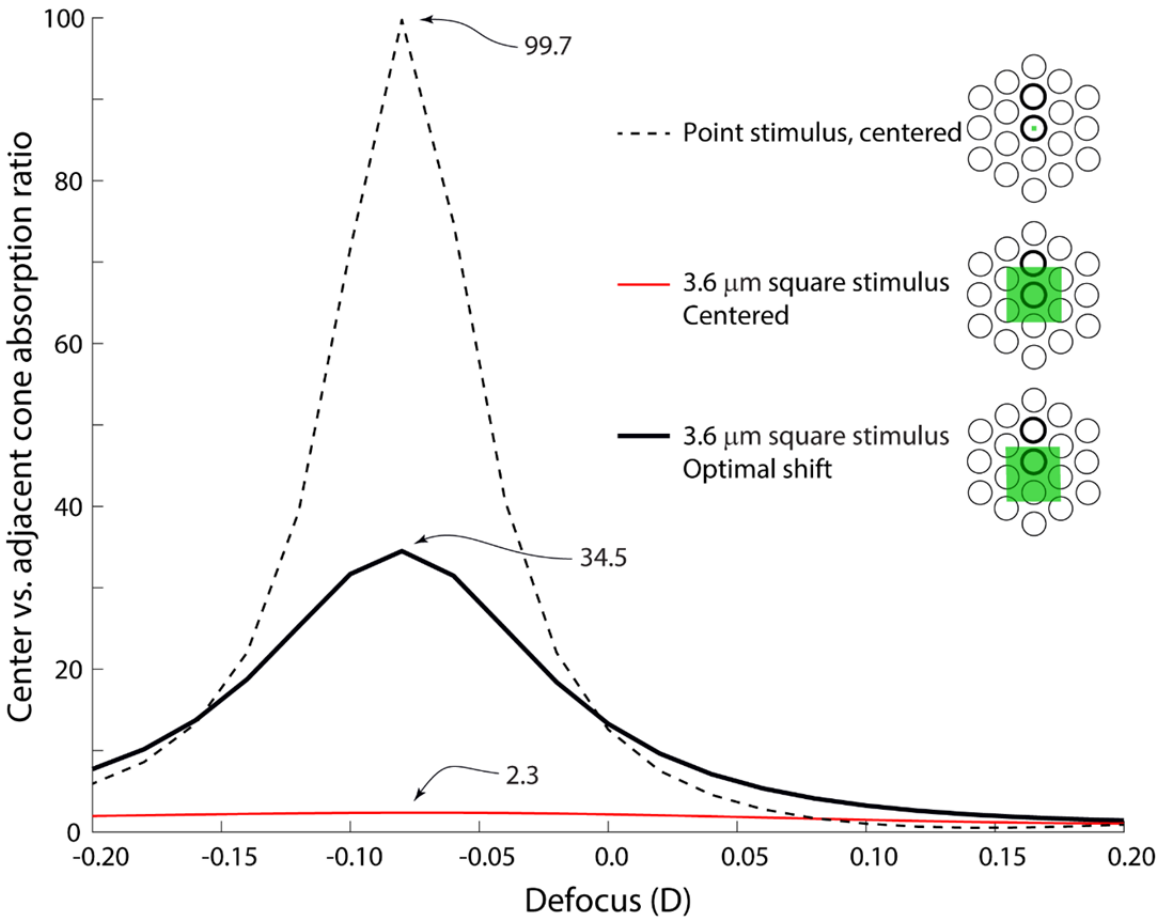

Figure 4. Ratio of light capture for adjacent foveal cones as a function of defocus. Foveal cones were modeled with a 2 μm inner segment diameter at the ELM. Three stimulus configurations are shown: a point stimulus (dotted line), a centered 5×5 pixel stimulus (red line), and an optimally positioned 5×5 pixel stimulus (black line). The ratio compares the power absorbed in the center cone vs. the upper adjacent cone (heavy outlines in schematic at right). Best focal position in all cases is at -0.08 D relative to the ELM, which is ~24 μm inside the inner segment. Stimuli are depicted to scale but do not include transvers blurring by the point spread function, which causes the lowered ratio in the centered 5×5 stimulus case (as used in Experiment 3). The point stimulus is theoretical for reference purposes, but is not realizable in the retinal microstimulator.

GENERAL METHODS

Description of AOSLO Function

Adaptive optics scanning laser ophthalmoscopy (AOSLO) has changed how scientists can investigate the retina in an intact living eye. AOSLO retinal imaging can provide optical resolution better than of 2 μm, sufficient to make measurements of cellular and sub-cellular details of retina structure and function that were previously only achieved in either histological specimens tissue or in animal physiological preparations.

The 6 main components of an AOSLO are (1) light delivery optics, (2) wavefront compensation optics, (3) raster scanning mirrors (4) wave front sensors, (5) light detectors, and (6) image recording (Roorda *et al*., 2002). Here I will briefly outline the operation of each of these components in the AOSLO system used in our Experiments (Fig. 5).

(1) Light delivery: The light from a supercontinuum laser (NKT Photonics, Denmark) is split into 3 channels (green: 543 ±11 nm; red: 710 ± 10 nm; and infrared: 840 ± 25 nm for imaging and visual stimulation [at the powers used, 840 nm is readily perceived by subjects]) that are each coupled to single mode optical fibers. The tip of each fiber provides a point source, which is then all collimated into a single beam using dichroic mirrors. The entrance pupil diameter is set by an aperture placed after the beams are combined. This pupil is relayed by mirror telescopes to a deformable mirror, then relayed again through a pair of horizontal and vertical scanning mirrors, and finally to the

eye. Mirrors are used throughout the instrument to keep the system compact, to limit chromatic dispersion, and to avoid back reflections. The downside of using the mirrors is that astigmatism is created when they are used off axis. To partially compensate for the astigmatism, parts of the beam path travel in a Z plane. Sphere and cylindrical correction can be placed at the spectacle plane of the eye to minimize the higher order aberration correction required. Neutral density filters can be placed before the 3 beams are combined to independently control light levels at the imaging plane.

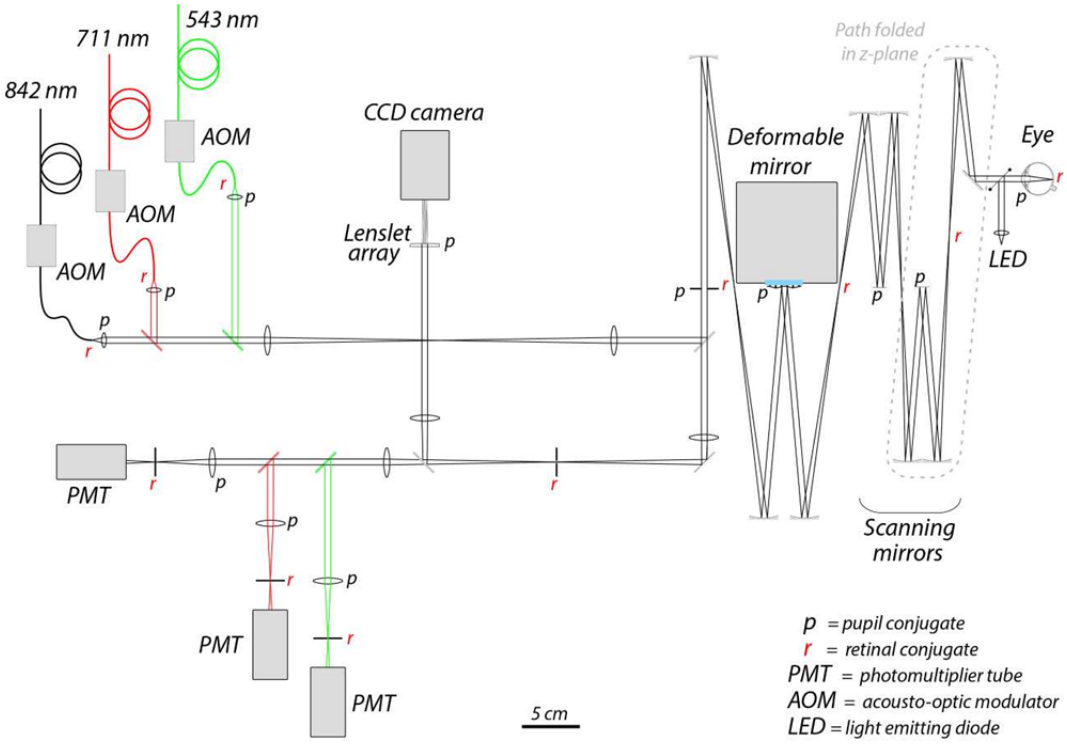

Figure 5. Optical schematic of the multi-wavelength retinal microstimulator. Light of three different wavelengths (split from the supercontiuum laser source, not shown) is delivered via single mode fibers, each with independent highspeed fiber-coupled modulators (light levels can be controlled pixel-by-pixel over a 10-bit modulation depth). Wave front sensing is measured over a 6 mm pupil with a Shack-Hartmann style sensor, made with a lenslet array and CCD camera. Wave front correction is done at 30 Hz in closed loop, with a 5.5 µm stroke MEMS deformable mirror. Raster scanning of the retina is produced with a 16 kHz resonant scanner coupled with a variable rate vertical scanner (to allow frame rates to be changed, although 30 Hz is typical). Independent photomultiplier tubes are used for detection of each light source, and video images from each wavelength can be generated. Lateral and axial positions of the light sources and the

detectors are adjusted to make all sources and detectors conjugate to a single point on the retina (chromatically corrected longitudinally for each wavelength). Pupil conjugate and retinal conjugate positions are indicated as *r* and *p* throughout the optical path. Layout is to scale.

(2) Raster scanning: The beam is traverses the retina with a resonant and galvanometric scanner combination. The resonant scanners scan the beam vertically at 16 kHz in a sinusoidal pattern, and it's frequency sets the timing signals for the rest of the electronic controls. The galvanometric scanner is synced to the resonant scanner and operates in a sawtooth pattern at $1/512^{th}$ of resonant scan frequency. Together the scanning mirrors provide 512 lines per frame at 30 frames per second. Both scanning mirrors are kept optically conjugate with the entrance pupil to ensure there is minimal movement of the scanning beam at its pivot point.

(3) Wavefront sensing: The wavefront aberration is measured with the same 840 nm light used for imaging. This is possible because the light scanned on the retina is descanned on the return path, rendering the beam stationary. As a consequence, the wavefront sensor registers the reflected light as though it was coming from a single spot, making aberration measurement possible. The aberrations are measured with Shack-Hartmann sensing made up of a square lenslet array of 24 mm focal length lenslets, each with a diameter of 400 μm. The sampled wave aberrations are fit to 10^{th} order Zernike polynomials.

(4) Wavefront compensation: Aberrations are corrected on both ingoing and outgoing light paths, using the Zernike coefficients to create a shape on the deformable mirror (144 actuator, 5.5 μm stroke deformable MEMS mirror, Boston Micromachines) that compensates for the measured aberrations. Correcting the wave aberrations on the way into the eye helps to focus the light to a diffraction-limited spot on the retina.

Correcting the aberration on the way out helps diffusely reflected light from the eye to be refocused to a compact spot in the confocal plane of the photodetector, resulting in higher axial resolution that blocks out-of-focus and scattered light from the retina. Wavefront correction operated in closed-loop mode at 16 Hz.

(5) Light detection: The descanned light from the retina is focused onto a confocal pinhole. The ideal pinhole diameter is 1.5 times the computed Airy disk diameter (for each wavelength), but here we increased throughput by using pinholes that were closer to 2 times the Airy disk diameter. The light passing through the pinhole is detected with a GaAs photomultiplier tube (Hamamatsu). The resulting voltages are fed to the analog inputs of a video board. The output of the photomultiplier tube combined with positional signals from the scanning mirrors are used to render a 512×512 pixel imaging video at 30 Hz. The frame grabber only digitizes pixels while the scanning beam is moving in the forward direction. All 512 pixels are acquired during the central 80% of the extent of the fast scan. The sinusoidal distortions associated with this scan are removed from the acquired images digitally using a procedure employing a calibrated imaging grid.

Experimental Methods

For all of our studies subjects used a dental impression mount affixed to an X-Y-Z translation stage to set and maintain eye position during the experiment. The retinal location of the wavefront correction and imaging was controlled by having the subject view a point fixation target through a pellicle beamsplitter. Wavefront correction and imaging was done through a 5.6 mm pupil. One drop of 0.5% tropicamide and one drop

of 0.1% cyclopentolate was instilled 30 min prior to imaging to dilate the pupil and minimize accommodative fluctuations. Additional experiment details on the psychophysical tasks are described in Results. To illustrate that the AOSLO was able to generate 0.02 D focal steps, we imaged one retina over a series of 13 defocus positions (Fig. 6). This series illustrates how small focal changes lead to noticeable differences in the sharpness of the imaged cones (judged by image contrast). In this example, the sharpest cones appeared with a defocus value of -0.16 D (a value related to the LCA correction imposed by the instrument being designed to be emmetropic at 710 nm rather than the 840 nm light imaged here).

Independent 10 bit modulation of the imaging and stimulus channels was achieved by passing them through dedicated acousto-optic modulators (AOMs) operating at 50 MHz before their entry into the scanning and corrective portions of the optical path. High speed switching allows custom stimuli to be delivered to the retina, in pixel by pixel correspondence with the acquired image. Because pixel position and time are linked in scanning system, a digital marker is placed in the retinal video on the pixel location corresponding to the time of AOM triggered stimulus delivery. All imaging and psychophysical testing was conducted using a 5.6 mm system pupil and 1.28° imaging field (400 image pixels per degree of visual angle). One pixel therefore equaled 0.15 arcmin, or ~0.72 microns on the retina.

Retinal imaging and light delivery was performed in one eye of 3 adult subjects with normal vision and color perception (2 males aged 20 and 55, and 1 female aged 29). Mydriasis and cycloplegia was achieved by instilling 0.5% tropicamide and 1% cyclopentolate 30 minutes before testing. A head worn eye patch was used to occlude the

fellow eye. Trial lenses were introduced in the optical path if needed to minimize low order ocular aberrations. Psychophysical experiments required steady fixation on a small masked LED light source viewed through a pellicle beam splitter. Retinal stimulation sites were chosen near the horizontal meridian temporal from fovea, as determined from a large montage of initially acquired AOSLO images. Images of the vasculature were generated using AO-based techniques (Tam *et al.,* 2010) and a test site was chosen, if possible, from capillary-free regions to avoid interference by blood vessels.

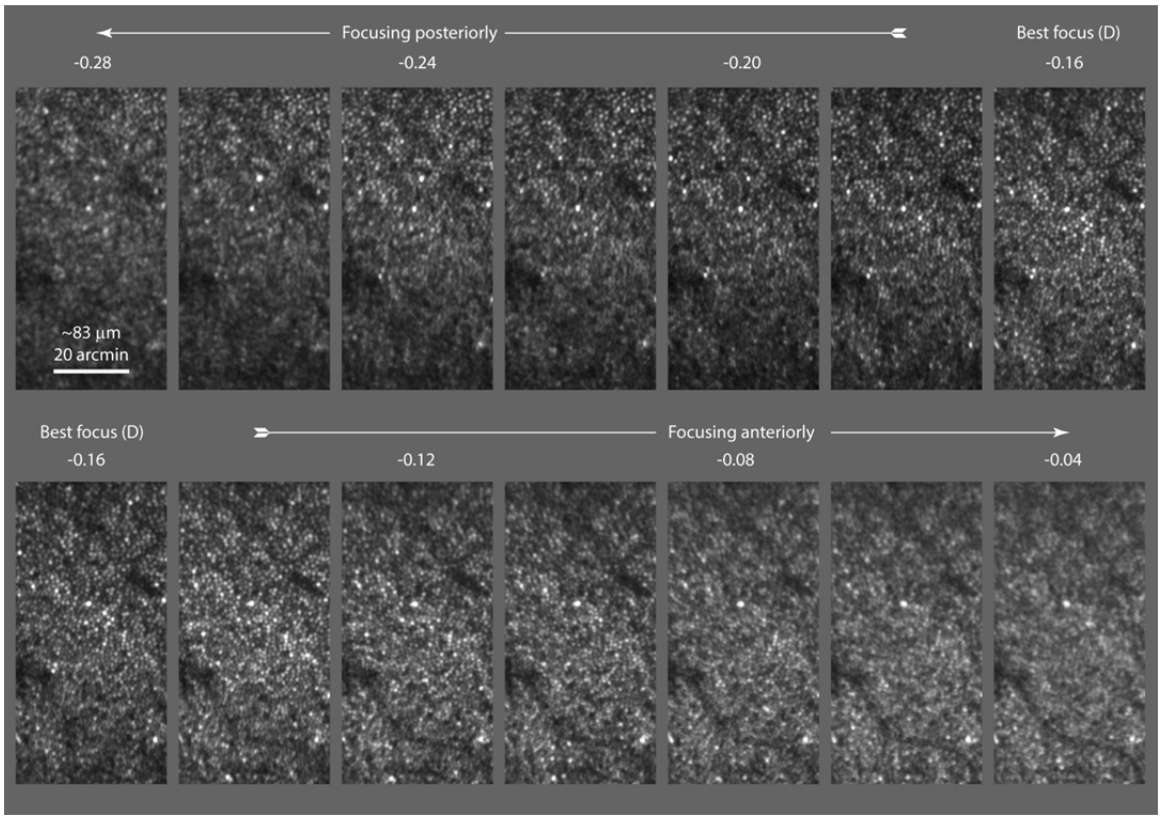

Figure 6. Appearance of the retinal cone mosaic at ~1° eccentricity with different focal imaging planes in an AOSLO. The images show how the appearance of cones vary with small focal changes. The top row of images shows focal changes done posteriorly starting from the best focus. The bottom row of images shows the variation of cones when the focal changes are done more anterior from the best focus. Subject 147L. Field width in each panel is 35 arcmin.

RESULTS

Our aim was to determine how small a defocus step humans are sensitive to using psychophysical techniques. Adaptive optics corrected stimuli enabled us to make focus steps on the order of 0.02 D. Stimuli were delivered under interleaved conditions with variable defocus steps, and subjects were asked to assess either sharpness or brightness of grating or spot stimuli. Measuring sensitivity to microfocal changes should help us to determine where in the retina the best focus is located axially.

Because defocus sensitivity has not been tested with stabilized AO-corrected stimuli previously, we conducted several different preliminary experiments to determine which approach was best able to measure microfocal effects. In the 3 experiments detailed below, the first two were essentially pilot experiments where we discovered that it was impractical to be able to quantify the small changes in defocus that we sought. Nonetheless, I am reporting all of these data in order to give the reader a sense of the advantages and disadvantages of each of the approaches we took.

Experiment 1

Methods and Results

In this experiment a static stimulus was presented parafoveally in one of two focal positions, and the subject was asked to report which of the two stimuli appeared sharper. This is a two-alternative forced choice design, with each single stimulus appearing

sequentially. One subject viewed a continuously presented checkerboard stimulus (25×25 or 16×16 pixels subtending ~0.25° at 400 pixels/deg) displayed with no stimulus stabilization to compensate for fixational eye motion. The focal position of the stimulus was randomized for each trial. The subject used a bite bar to stabilize the head and fixated on a target light at ~1° temporally on the horizontal meridian (Fig. 7). The imaging was conducted with an instrument focus of -0.2 D (for best cone imaging; note that this focus offset is due to instrument requirements to correct for longitudinal chromatic defocus between the infrared and green light). The responses to the set of trials for each run are given here:

> Experiment 1.1: 25×25 pixel stimulus (Stimulus A in Fig. 7), choice between -0.2 and -0.28 D. Subject chose -0.2 D as best focus 3 out of 4 times.
>
> Experiment 1.2: 16×16 pixel stimulus (Stimulus B in Fig. 7), choice between -0.2 and -0.12 D. Subject chose -0.2 D as best focus 3 out of 4 times.

These data show that the subject could discriminate the focus of a stimulus at 1° eccentricity with defocus step sizes of 0.08 D.

We next tried a similar experiment to achieve smaller focal step discrimination. We used a finer grid and included a presentation at the fovea condition. This was also a two-alternative forced choice task, but with a 0.04 D step size difference between the two conditions. The one subject viewed a 4×4 pixel checkerboard stimulus (subtending ~0.25° at 400 pixels/deg) with no stimulus stabilization. Subject used a bite bar, and fixated on a target light at ~1° or simply foveal judgment. There was no correction for any fixational eye motion. The data for these two runs are given here:

> Experiment 1.3: At fovea with Stimulus C (Fig. 7), with adaptive optics closed loop off, randomized choice between -0.2 and -0.16 D. Subject chose -0.2 D as best focus 3 out of 3 times.

Experiment 1.4: Fixation at ~1° with Stimulus C (Fig. 7), with adaptive optics closed loop off, randomized choice between -0.2 and -0.16 D. Subject chose -0.2 D as best focus 4 out of 4 times.

These data show that a subject can detect axial focal changes as small as 0.04 D.

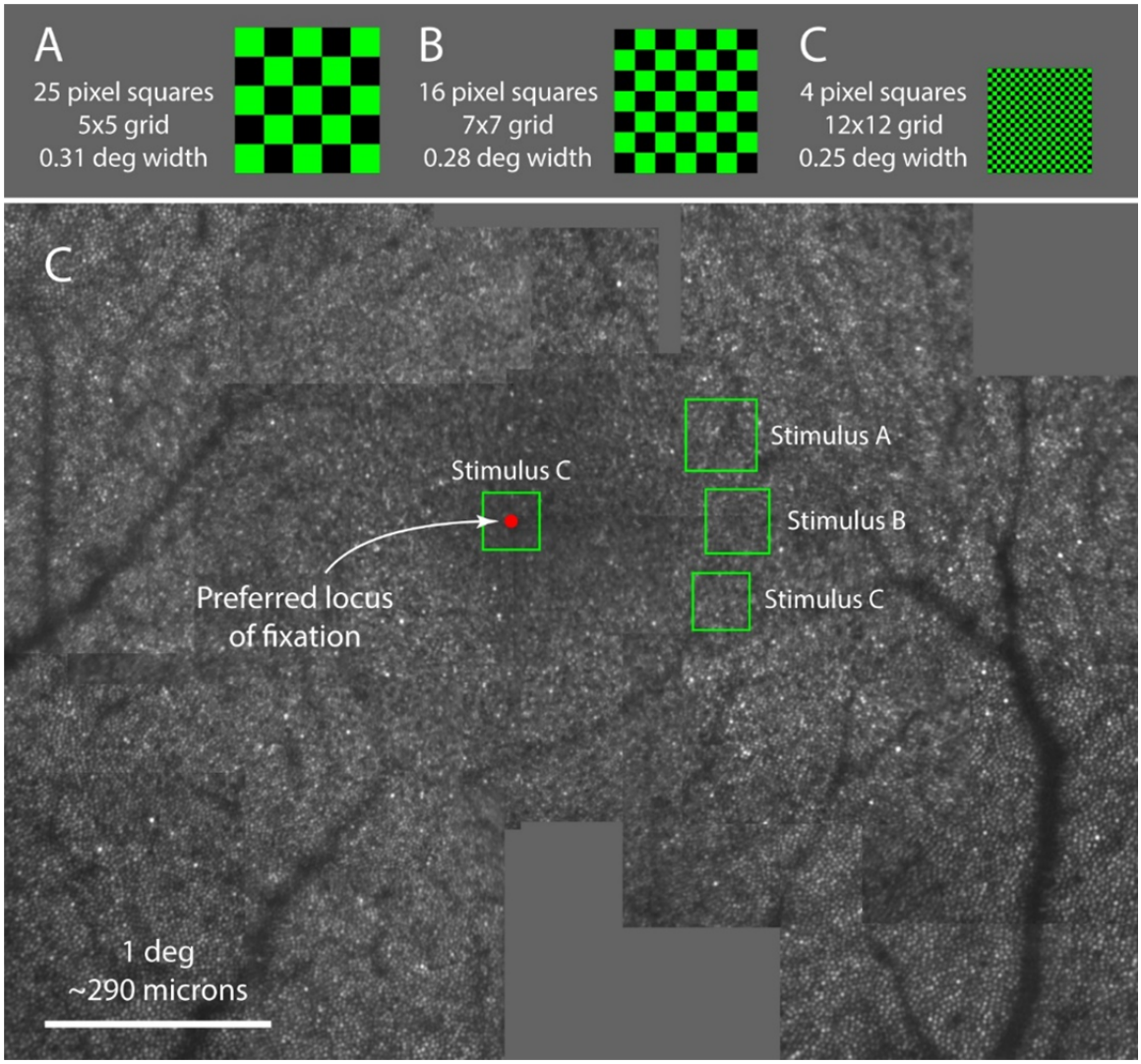

Figure 7. *Stimuli and retinal loci used in Experiment 1.* The above figure shows retinal montage where the green box is showing the size and location of each stimulus. Red dot indicates subject's preferred retinal locus of fixation, determined by having the subject fixate on a small flashing spot during a separate imaging session. Subject 147L.

Discussion

The subject reported that the task was difficult and was unlikely to be useful for attaining measurements that could reliably test smaller defocus steps or to measure the location of the peak sensitivity as this would have required an impractically large number of trials. Another disadvantage was that AO correction could not be run in closed-loop, which meant that the AO correction was not updated during small changes in fixational eye position. A final disadvantage here was that the smallest checkerboard pattern probably did not allow sufficiently cone contrast to be sensed as there was essentially no spacing between stimulus checks. Because we were interested in finding the focal position with the peak light capture, these two disadvantages lead us to try Experiment 2.

Experiment 2

Methods and Results

A more direct measure of light capture in photoreceptors is to use flashed stimuli and measure increment thresholds. In this experiment we used flashed line or spot stimuli with Quest thresholds, a standard staircase method used previously in an AOSLO (Harmening *et al.*, 2014). For all the experiments detailed below, a single run entailed a series of 20 trials where the intensity of the stimulus varied depending on the response history of the subject. At the end of each run, a single estimate of threshold was calculated. We ran 3 staircases across 3-5 focal positions in an attempt to measure where the lowest detectable light level would be, which is would be equivalent to the peak light

capture efficiency. As shown in Fig. 8, we tried 4 variations of this experiment in one subject, outlined in turn:

Experiment 2.1: The subject viewed three 1 pixel wide lines, spaced 8 pixels apart, and 51 pixels high. Fig. 8A shows the stimulus on the retinal site tested, with eccentricity noted. The stimulus was present for during 30 frames (1 sec) on each trial. The Quest algorithm is a staircase of 20 trials, and one such staircase is shown in Fig. 8B. We did this 3 times at each of 3 defocus values (Fig. 8C). The data did not shown any effect of focal position. However, we noted that stimulus stabilization was not good with a long presentation time, and this could have compromised the result.

Experiment 2.2: The subject detected one 5×5 pixel square (Fig. 8D), presented for 1 frame (33 msec). One Quest staircase is shown in Fig. 8E. Here we did 5 focal positions (Fig. 8F), and again did not see evidence of a peak focal position in these data. Because the stimulus primarily stimulated one cone, noise level expected in such a measurement may have been too great to detect the small changes in defocus.

Experiment 2.3: To engage more cones in the task, we next tried an extended stimulus of two 1 pixel wide lines, spaced 8 pixels apart and 31 pixels high (Fig. 8G). The stimulus was presented for 1 frame on each trial, in the same location as in Exp. 2.2. Again, the threshold data measured across 5 focal positions did not reveal a clear trough of sensitivity (Fig. 8I). At this eccentricity the stimulus only impinged on a small number of cones, which may have limited the outcome due to perceptual noise.

Experiment 2.4: We next extended the stimulus further, to three 1 pixel wide lines, spaced 8 pixels apart and 31 pixels high. As earlier, the stimulus was presented for

1 frame on each trial. In this experiment, we were at 2.8° eccentricity, and again we did not detect a clear trough of sensitivity across 5 focal positions (Fig. 8L).

Discussion

This series of experiments appeared to be limited by measurement noise. Based on the optical modeling data shown in Fig. 3, there is a difference in light capture between the peak value (at -0.06 D) and the low point (at 0.15 D) of about 22% (for all cones, dashed line). The scatter in our measurements here is sometimes larger than 22%, suggesting that increment thresholds may not be sensitive enough to reveal the focal discrimination we predict from the model. Some of the experimental noise is also likely to be due to residual uncorrected aberrations. Finally, for Experiments 2.2-2.4, the number of total number of trials for an experiment was 20×3×5 = 300 which is at the upper end of the number of trials that a subject can conduct reliably, based on experience in the lab.

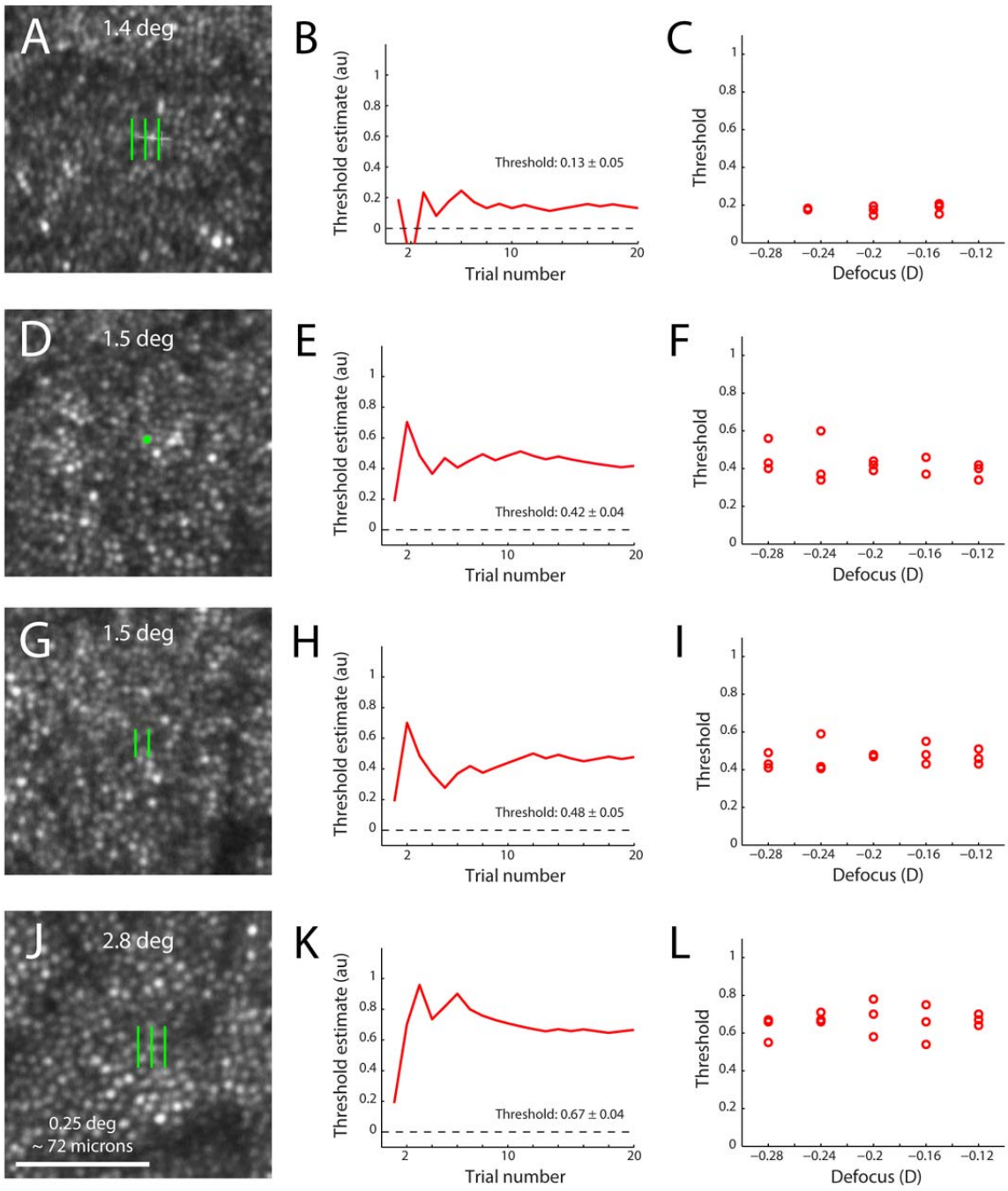

Figure 8. *Data from Quest increment threshold studies.* Retinal montages (left column), example single threshold estimates (middle column) and repeat threshold estimates as a function of defocus (right column) derived from Experiments 2.1 – 2.4.

Experiment 3

Methods and Results

Because acuity is naturally best during sustained foveal viewing, we designed an experiment to test defocus sensitivity at the fovea using a method of adjustment. Here the stimulus was presented continuously with AO correction, but without stabilization. The stimulus was a set of small spots arranged in a hexagonal grid pattern. The spacing between spots was wide enough to include 1-2 cones when viewed at the fovea. This should allow the light capture between neighboring cones to reach high contrast levels (as shown in Fig. 4). The subject was tasked with looking at the stimulus and adjusting the focus (using the arrow keys on a keyboard) until he/she felt the stimulus was as sharp as they could perceive it to be (we did not ask the subject to judge "contrast" because it is not as intuitive a concept for subjects as "sharpness"). There was no time limit on making this judgment. At the beginning of each trial, the operator set the instrument focal position at random, within a range that did not corrupt the AO correction. The operator then informed the subject that they could begin adjusting the focus. This was done with a green stimulus in one series of trials, followed by a second series with a "negative" infrared stimulus as a series of trials (which appear as a group of black spots on a red background, see Fig. 9). Two of the 3 subjects were naïve to AO psychophysics (122R and 123R). Subjects and their results are detailed individually below.

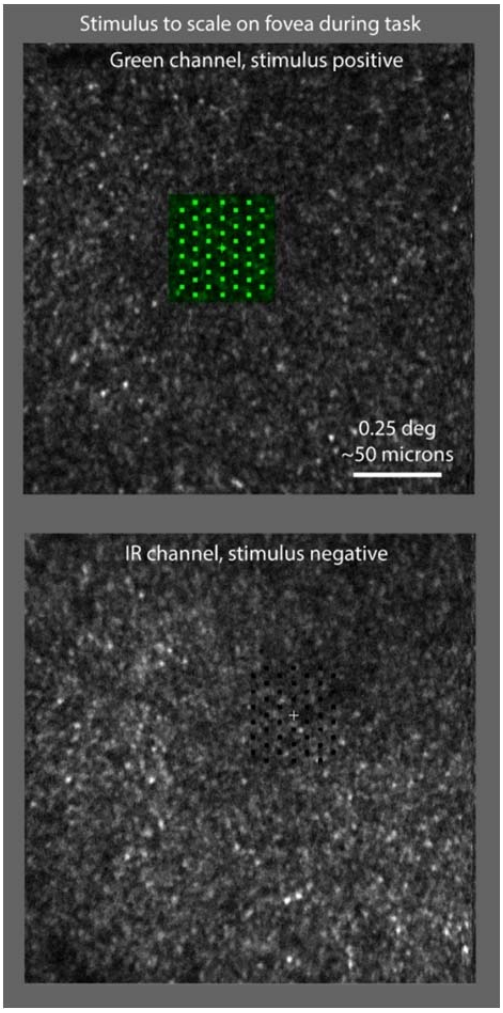

Figure 9. Schematic representation of stimulus pattern for Experiment 3. Panels show the retinal image of the fovea of Subject 122 with a 543 nm green stimulus (top) or the 840 nm negative infrared stimulus (bottom) which appear as a group of black spots. Stimuli are to scale relative to the AOSLO image.

Subject 147L (male, 55 years old). Stimulus was a group of 5×5 pixel squares arranged in a hexagonal pattern (as shown in Fig. 9). This stimulus subtended 96 pixels in width and 110 pixels in height, equivalent to 14.4 × 16.5 arcmin. Figure 10 shows that the subject selected distinct focal positions for the green and infrared stimuli, with a standard deviation of less than 0.02 D for each wavelength.

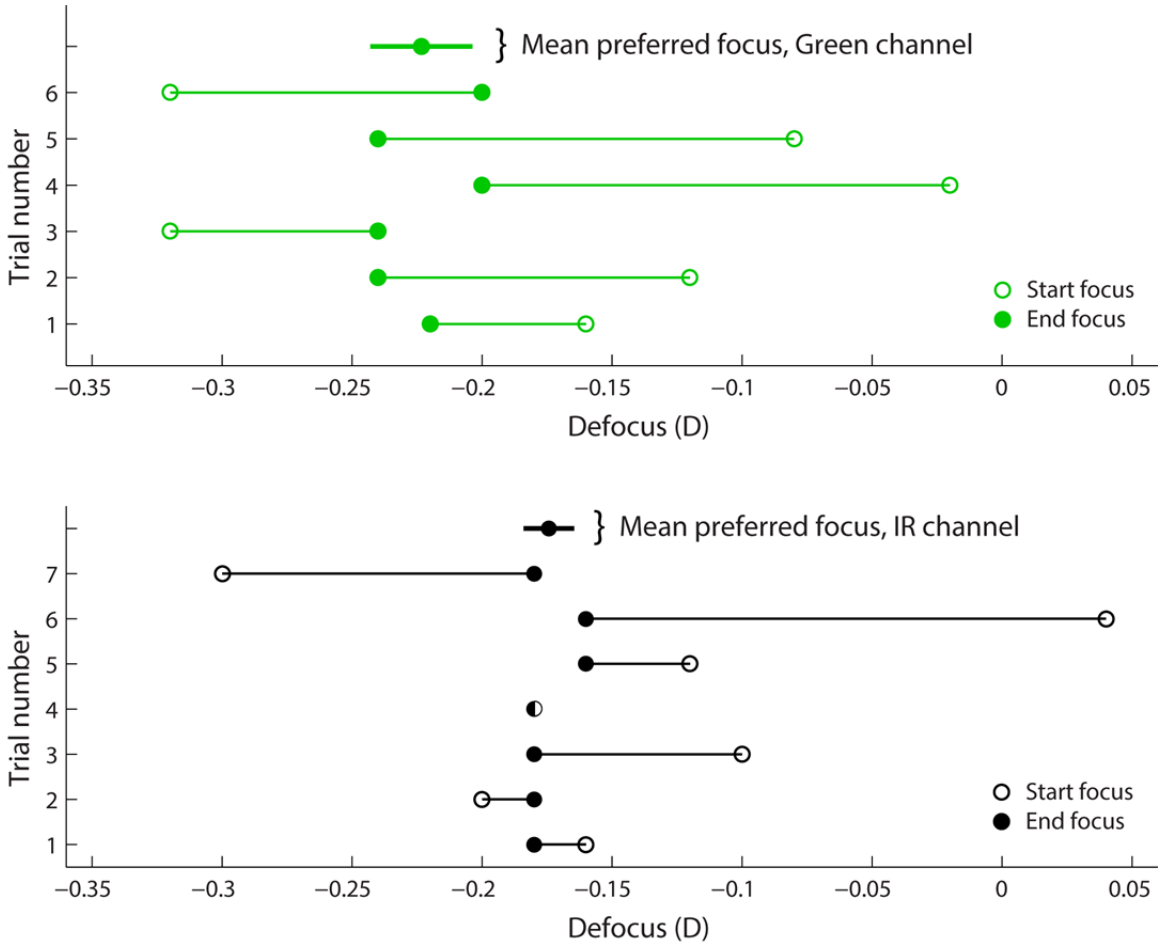

Figure 10. Data showing that the mean preferred focus for Subject 147L in the green channel was -0.223 D (±0.0197 SD) and for the infrared channel was -0.174 D (±0.0098 SD). Defocus values are instrument settings, not model predictions.

Subject 122R (female, 29 years old). Stimulus was a group of 5×5 pixel squares arranged in a hexagonal pattern in the green channel (same stimulus as with Subject 147L in the green channel). In the infrared channel, we had to switch to a larger stimulus: 7×7 pixels squares in a hexagonal pattern, subtending 116×117 pixels (width × height), equal to 17.4 × 17.55 arcmin. Figure 11 shows that this subject had similar mean preferred focal positions for both wavelengths, with a standard deviation averaging 0.025 D.

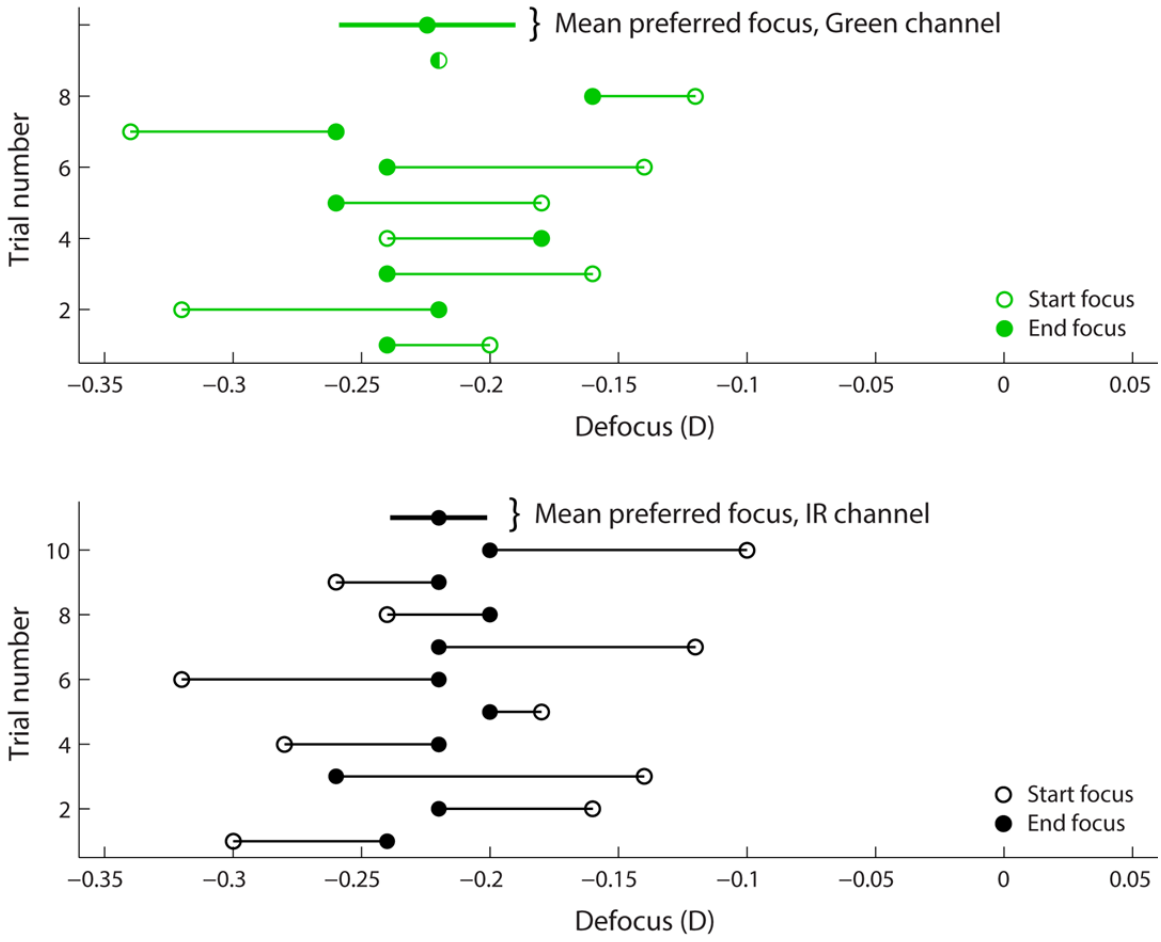

Figure 11. Data showing that the mean preferred focus for Subject 122 R in the green channel was -0.224 D (±0.0343 SD) and in the infrared channel was -0.220 (±0.0189 SD). Defocus values are instrument settings, not model predictions.

Subject 123R (male, 20 years old). Stimulus pattern for both green and infrared channels was a 7×7 hexagonal grid of squares, subtending 116×117 pixels (width × height), equal to 17.4 × 17.55 arcmin. Figure 12 shows that this subject exhibited different mean preferred focal positions for each wavelength, with a standard deviation averaging 0.020 D. The large difference in preferred focal positions suggests that this subject may have had longitudinal chromatic disparities that differed from the theoretical values set in the AOSLO instrument (see Discussion).

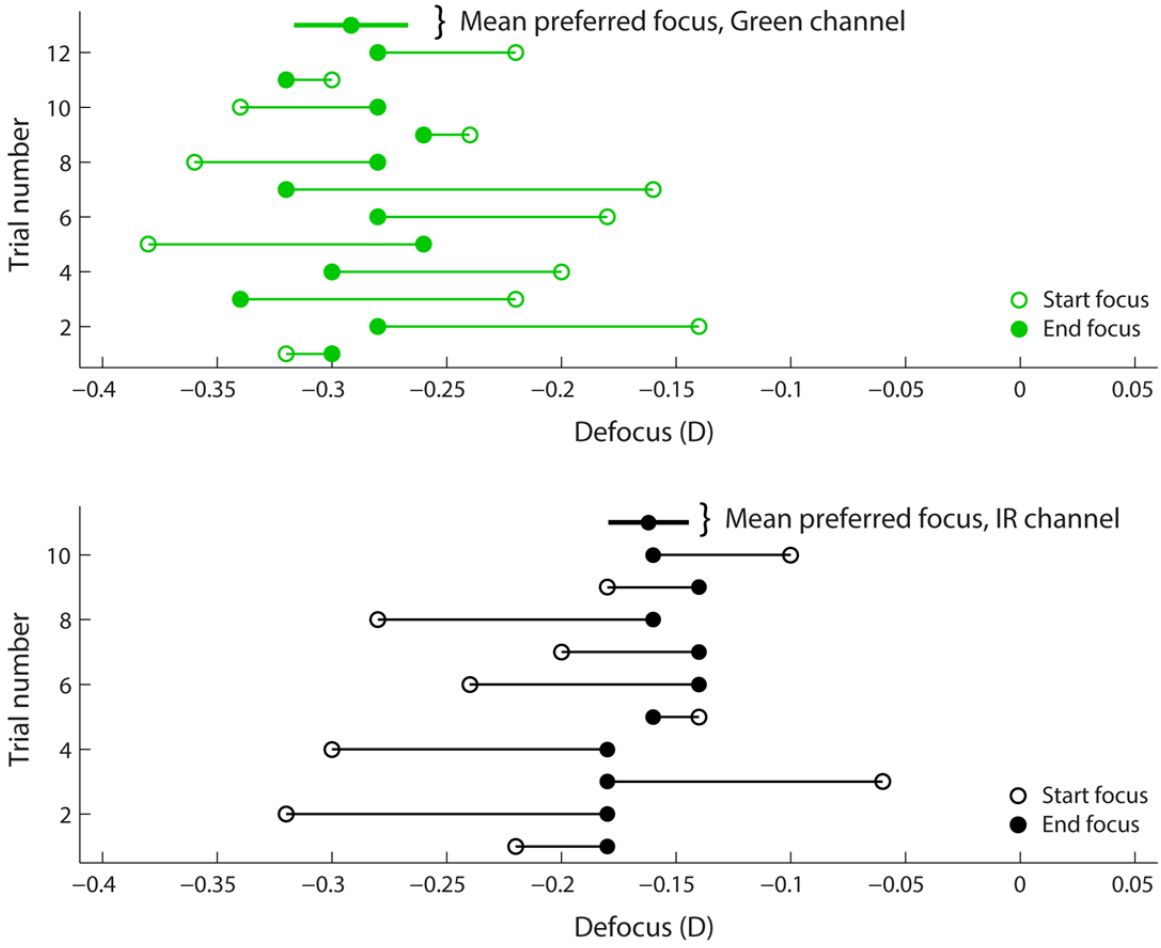

Figure 12. Data showing that the mean preferred focus for Subject 123R in the green channel was -0.292 D (±0.0248 SD) and for the infrared channel was -0.162 D (±0.0175 SD).

DISCUSSION

My primary finding was that normal subjects can determine an optimal focal position to judge image sharpness at the fovea with an accuracy of about 0.02 D for a given wavelength when high-order aberrations have been corrected with adaptive optics. This dioptric distance is equivalent to ~6 μm in axial depth, which is much shorter than the typical length of a human foveal cone of 60-70 μm. Such microfocal sensitivity suggests that light capture efficiency is not simply determined by the length of the cone outer segment (~35 μm at the fovea) where all the photopigment is likely to be equally sensitive to light. Here I discuss several issues raised by the results, namely: (1) how waveguiding may heighten peak light capture axially, (2) why the different wavelengths lead to different best focal positions, and (3) is it possible to pinpoint the absolute focal position in the retina that is the starting point for defocus sensitivity.

If photoreceptor wave guiding effectively sets light capture, stimuli should be most easily seen as in focus when it leads to the highest contrast in light capture between neighboring cones. The foveal cone model outlined in Fig. 2 predicts that peak light capture in just one cone occurs at a focal position of -0.08 D relative to the ELM, which is inside the inner segment. For determining contrast between foveal cones, we estimated the contrast for different focal positions in combination with different stimulus locations (Fig. 4). This was required because the stimuli in Experiment 3 were presented continuously, fixed in visual space, which meant that the small green squares were

sliding across the cone mosaic due to fixational eye motion. Cone contrast would be low when a square was centered on one cone (red line in Fig. 4), while it would be maximal when the edge of a square landed between cones (black line in Fig. 4). It appears from the subject responses that the focus judgment was being driven by the latter condition because the standard deviation in the focal position was 0.02 D, which is less than the half-width of the optimal stimulus position of ~0.04 D. Waveguiding contributes to this effect because the best focal position prevents the most light from entering neighboring cones (see Fig. 2). It is also noteworthy that the defocus sensitivity is better than predicted for a single stimulus. Because our subjects were presented with a hexagonal grid of spots, this suggests that the focus decision may have relied on the integrated input from many cone contrast signals as the spacing between spots was wide enough to include 1-2 cones when viewed at the fovea. Our results are consistent with the idea that neighboring cone contrast at the fovea helps set the acuity limit under AO corrected conditions (Rossi & Roorda 2010).

Two subjects showed different preferred focal positions for green versus infrared light compared to one subject (122R) that had similar preferred focal positions. The differences in preferred focal positions suggests that some subjects may have had longitudinal chromatic disparities that differed from the theoretical values set in the AOSLO instrument (derived from Atchison & Smith 2005). In Subject 147L the defocus difference between wavelengths was 0.049 D, and for Subject 123R it was 0.130 D. These differences are within range of measurement error for LCA in human subjects (Thibos et al., 1992). Thus it is not surprising that uncorrected residual LCA differences would be present among our subjects. To have eliminated such differences in each

subject would have required modifying the focal conjugates for each wavelength for each subject, a task that could be done but was impractical for the present experiments.

Finally, it is clear that one limitation of our results is that we were not able to measure the absolute focal position of the best focus in Experiment 3, instead we have a relative focal point for a given wavelength. Having a relative value means we cannot directly link the focal position found in our subjects to the predicted location of maximum light capture in the cone model (Figs. 2-3). Even if we were able to identify the absolute focal position for best focus psychophysically, it may still deviate from the model predictions due to a number of factors that may influence light capture. Most likely would be various sources of intraocular scatter, like the stray light that arises from the cornea, lens, vitreous humor, and retinal tissue lying in front of the photoreceptors. These scattering sources cannot be sensed or controlled by AOSLO and therefore may lead to compromised relative light capture between adjacent cones compared to the diffraction-limited model.

One way that it might be possible to determine the absolute focus position would be to use the reflected light images as a gauge. Waveguiding is equally effective for light reflected back through photoreceptors, since optical systems are reversible. The cones are generally thought to have two major reflective structures: the anatomic junction between the inner and outer segment, and the junction between the outer segment and its contact with retinal pigment epithelium. Development of a model of reflected light propagation could possibly be used to estimate what the AOSLO images should look like from specific focal positions (Meadway & Sincich 2018b). The idea would be to image cones with different focal positions and see if reflected model images correspond to the images

taken at the perceptual best focus. Such an approach may be a useful future extension of the light propagation model in order to reveal where in the depth of the retina light achieves its optimal capture.

REFERENCES

Artal P (2016). "The Eye as an Optical instrument". Chapter 12 from *Optics in Our Time,* Mohammad D. Al-Amri, Mohamed El-Gomati, M. Suhail Zubairy. DOI 10.1007/978-3-319-31903-2_12.

Atchinson DA and Smith G (2000). *Optics of Human Eye*, Oxford, UK: Butterworth Heinemann.

Atchison DA and Smith G (2005). Chromatic dispersions of the ocular media of human eyes. *J. Opt. Soc. Am.* A 22(1):29–37.

Burns SA, Wu S, He JC & Elsner AE (1997). Variations in photoreceptor directionality across the central retina. *Journal of the Optical Society of America A* 14:2033–2040.

Campbell FW and Westheimer G (1960). Dynamics of accommodation responses of the human eye. *J Physiol* 151:285-295.

Charman WN, Whitefoot H. (1977). Pupil diameter and the depth of field of the human eye as measured by laser speckle. *Optica Acta*. 24:1211–6.

Chen L, Kruger PB, Hofer H, Singer B, Williams DR. (2006). Accommodation with higher order monochromatic aberrations corrected with adaptive optics. *J Opt Soc Am A Opt Image Sci Vis*. 23 (1):1-8.

Curcio CA, Sloan KR, Kalina RE, Hendrickson AE (1990). Human photoreceptor topography. *J Comp Neurol* 292:497-523.

Curcio CA, Sloan KR (1992). Packing geometry of human cone photoreceptors: variation with eccentricity and evidence for local anisotropy. *Vis Neurosci*. 9(2):169–180.

Chui TY, Song H, Burns SA (2008). Adaptive-optics imaging of human cone photoreceptor distribution. *J Opt Soc Am A Opt Image Sci Vis*. 25(12):3021–3029.

Enoch JM (1961). Wave-guide modes in retinal receptors. *Science* 133: 1353–1354.

Enoch JM, Tobey FLJ (1981). *Vertebrate photoreceptor optics*. Berlin: Springer.

Glasser A (2011). "Accommodation", Chapter 3 in *Adler's Physiology of the Eye*, Levin LA, Nilsson SFE, Hoeve JV (eds.), St Louis, US: Saunders.

Harmening WM, Tuten WS, Roorda A, Sincich LC (2014). Mapping the perceptual grain of the human retina. *Journal of Neuroscience*. 34 (16):5667-5677.

Harmening WM, Tiruveedhula P, Roorda A, Sincich LC (2012). Measurement and correction of transverse chromatic offsets for multi-wavelength retinal microscopy in the living eye. *Biomedical Optics Express* 3(9):2066-2077.

Hendrickson, AE and Yuodelis C (1984). The morphological development of the human fovea. *Ophthalmology* 91: 603-612.

Hirsch J and Curcio CA (1989). The spatial resolution capacity of human fovea. *Vision Res* 29:1095-1101.

Kotulak JC (1986). The accommodative response to subthreshold blur to perceptual fading during the Troxler phenomenon. *Perception* 15:7-15.

Ludlam WM, Wittenberg S, Giglio EJ, Rosenberg R (1968). Accommodative responses to small changes in dioptric stimulus. *Am J Optom Arch Am Acad Optom* 45:483-506.

Meadway A and Sincich LC (2018). Light propagation and capture in cone photoreceptors. *Biomedical Optics Express* 18:5543-5565.

Meadway A and Sincich LC (2018b). A model of cone photoreceptor reflectivity. *Association for Research and Vision in Ophthalmology Meeting*, 4631-A0273.

MacLeod DI, Williams DR, Makous W (1992). A visual nonlinearity fed by single cones. *Vision Res* 32:347–363.

Miller WH & Snyder AW (1973). Optical function of human peripheral cones. *Vision Research* 13:2185–2194.

Polyak SL (1941). *The Retina*. Chicago: University of Chicago Press.

Polyak SL (1957). *The Vertebrate Visual System*. Chicago, Illinois: University of Chicago Press.

Packer O, Hendrickson AE and Curcio CA (1989). Photoreceptor topography of the retina in the adult pigtail macaque (Macaca nemestrina). *Journal of Comparative Neurology* 288:165–183.

Remington LA (2012). *Clinical Anatomy and Physiology of the visual system*. 3rd edition. St. Louis: Elsevier/Butterworth-Heinemann.

Roorda A (2011). Adaptive optics for studying visual function: a comprehensive review. *J Vision* 11(7):1-21.

Roorda A, Romero-Borja F, Donnelly III WJ, Queener H (2002). Adaptive optics scanning laser ophthalmoscopy. *Optics Express* 10:405-411.

Rossi EA, and Roorda A (2010). The relationship between visual resolution and cone spacing in the human fovea. *Nat. Neurosci*. 13(2), 156–157.

Rodeick, RW (1973). *The Vertebrate Retina: Principles of Structure and Function*. San Francisco, CA: W.H. Freeman and Company.

Rowe MP, Engheta N, Easter SS, Jr. and Pugh EN, Jr. (1994). Graded-index model of a fish double cone exhibits differential polarization sensitivity. *Journal of the Optical Society of America* 11:55–70.

Sidman RL (1957). The structure and concentration of solids in photoreceptor cells studied by refractometry and interference microscopy. *Journal of Biophysical and Biochemical Cytology* 31:15–30.

Snyder AW & Pask C (1973). The Stiles-Crawford effect—explanation and consequences. *Vision Research* 13:1115–1137.

Salmon TO, Van de Pol C (2006). Normal Eye Zernike Coefficients and root- mean-square wave front errors. *J Cataract Refract Surg* 32:2064-2074.

Sincich LC, Sabesan R, Tuten WS, Roorda A, Harmening WM (2016). Functional Imaging of Cone Photoreceptors. In: Kremers J., Baraas R., Marshall N. (eds.) *Human Color Vision*. Springer Series in Vision Research, Vol 5. pp. 71-104, Springer: Cham.

Sincich LC, Zhang Y, Tiruveedhula P, Horton JC, and Roorda A (2009). Resolving single cone inputs to visual receptive fields. *Nat. Neurosci*. 12(8), 967–969.

Spaide RF, Curcio CA (2011). Anatomical correlates to the bands seen in the outer retina by optical coherence tomography. *Retina* 31:1609-1619.

Song H, Chui TYP, Zhong Z, Elsner AE, Burns SA (2011). Variation of cone photoreceptor packing density with retinal eccentricity and age. *Invest Ophthalmol Vis Sci*. 52(10):7376–7384.

Tam J, Martin JA, Roorda A (2010). Noninvasive visualization and analysis of parafoveal capillaries in Humans. *Invest Ophthalmol Vis Sci* 51:1691-1698.

Thibos LN, Ye M, Zhang X, Bradley A (1992). The chromatic eye: a new reduced-eye model of ocular chromatic aberration in humans. *Appl. Opt*. 31:3594-3600.

Thibos L, Hong X, Bradley A, Cheng X (2002). Statistical Variation Of aberration Structure and Image Quality in a normal population of Healthy eyes. *J Opt Soc Am A Opt Image Sci Vis* 19:2329-2348.

Wang B, Ciuffreda KJ (2006). Depth-of-Focus of the Human Eye: Theory and Clinical Implications. *J Surv Ophthal*. 51:75-85.

Wang B, Ciuffreda KJ (2005). Foveal blur discrimination of the human eye. *Ophthal. Physiol. Opt*. 25:45-51.

Williams DR (2011). Imaging single cells in the living retina. *Vision Res* 51, (13):1379-1396.

Westheimer G. (1967). Dependence of the magnitude of the Stiles Crawford effect on retinal location. *Journal of Physiology* 192:309– 315.

Yamada E. (1969). Some structural features of the fovea centralis of the human retina. *Archives of Ophthalmology* 82:151–159.

Zhang T, Godara P, Blanco ER, Griffin RL, Wang X, Curcio CA, Zhang Y (2015). Variability in Human Cone Topography Assessed by Adaptive Optics Scanning Laser Ophthalmoscopy. *Am J Ophthalmol*. 160(2):290-300.

APPENDIX

IRB APPROVAL LETTER

THE UNIVERSITY OF ALABAMA AT BIRMINGHAM
Office of the Institutional Review Board for Human Use

470 Administration Building
701 20th Street South
Birmingham, AL 35294-0104
205.934.3789 | Fax 205.934.1301 | irb@uab.edu

APPROVAL LETTER

TO: Sincich, Lawrence C.

FROM: University of Alabama at Birmingham Institutional Review Board
Federalwide Assurance # FWA00005960
IORG Registration # IRB00000196 (IRB 01)
IORG Registration # IRB00000726 (IRB 02)

DATE: 21-Dec-2017

RE: IRB-121221001
Perception of Visual Microstimuli

The IRB reviewed and approved the Continuing Review submitted on 18-Dec-2017 for the above referenced project. The review was conducted in accordance with UAB's Assurance of Compliance approved by the Department of Health and Human Services.

Type of Review: Full (Institutional Review Board 01 (UAB))
Determination: Approved
Approval Date: 20-Dec-2017
Approval Period: One Year
Expiration Date: 19-Dec-2018

Documents Included in Review:

- Sincich HSP
- Sincich 2017 consent clean
- Sincich 2017 consent stamped
- Response 16Dec2017
- Sincich 2017 progress report